Anisotropic nonsaturating magnetoresistance observed in $HoMn_6Ge_6$: A kagome Dirac semimetal

Achintya Low, Tushar Kanti Bhowmik, Susanta Ghosh, and Setti Thirupathaiah*
Department of Condensed Matter and Materials Physics, S. N. Bose National Centre for Basic Sciences, Kolkata 700106, India

(Received 22 January 2024; revised 8 March 2024; accepted 17 April 2024; published 1 May 2024)

We report the magnetic and magnetotransport properties and electronic band structure of the kagome Dirac semimetal $HoMn_6Ge_6$. Temperature-dependent electrical resistivity demonstrates various magnetic-transition-driven anomalies. Notably, a crossover from negative to positive magnetoresistance (MR) is observed at around 150 K. While the linear nonsaturating positive MR in the low-temperature region is mainly driven by the linear Dirac-like band dispersions as predicted by the first-principles calculations, the negative MR observed in the high-temperature region is due to the spin-flop-type magnetic transition. Consistent with anisotropic Fermi surface topology, we observe anisotropic magnetoresistance at low temperatures. A significant anomalous Hall effect has been noticed at high temperatures in addition to a switching of the dominant charge carrier from electron to hole at around 215 K.

DOI: 10.1103/PhysRevB.109.195104

I. INTRODUCTION

The combination of frustrated magnetism, strong electronic correlations, and quantum topology in kagome systems is immensely attractive to researchers from the point of view of fundamental science and potential technological applications [1–8]. Particularly, the interplay among these peculiar physical properties in the kagome lattice features intriguing quantum phenomena, including the quantum spin liquid phase [9–12], flat bands [13–16], Dirac and Weyl fermions [15,17–21], the Chern quantum phase [22,23], and a skyrmionic lattice [24,25]. So far, transition-metal-based kagome systems have been extensively explored to find the Weyl fermions in Mn_3Sn(Ge) [18,26], giant anomalous Hall effect in $Co_3Sn_2S_2$ [19], Nernst effect in Fe_3Sn [27], and skyrmion lattice in Fe_3Sn_2 [28]. On the other hand, the recent discovery of a nearly ideal quantum limit Chern magnet with massive Dirac fermion in $TbMn_6Sn_6$ has ignited an intense search for rare-earth-based kagome systems [23].

Following this discovery, several experimental reports appeared that discussed the tuning of topological properties in RMn_6Sn_6 (R = Gd–Tm, Lu) [29], the large anomalous Hall effect in RMn_6Sn_6 (R = Tb, Dy, Ho) [30], the Chern magnetic state in $TbMn_6Sn_6$ [23], Dirac-like band crossings in $HoMn_6Sn_6$ [31], and linear unsaturated magnetoresistance in RMn_6Sn_6 (R = Gd, Tm, Lu) [29]. Among these, $HoMn_6Sn_6$ is a ferrimagnetic metal in which the spins of the Ho $4f$ sublattice align antiferromagnetically with the spins of the Mn $3d$ sublattice. Thus, the interplay between the ferrimagnetism and the electronic band structure plays a vital role in shaping the linear nonsaturated magnetoresistance of this system [29,31,32]. On the other hand, although $HoMn_6Ge_6$ has a crystal structure similar to $HoMn_6Sn_6$, minimal information is available on the magnetotransport properties of $HoMn_6Ge_6$ and the relation between magnetic and magnetotransport properties [33].

$HoMn_6Ge_6$ crystallizes into a $HfFe_6Ge_6$-type hexagonal structure with a space group of $P6/mmm$, ordering antiferromagnetically at a Néel temperature of 466 K [34]. The magnetic moments of Mn and Ho are arranged in a skew-spiral ($\widetilde{SS}$) fashion, and the plane of magnetic moments (Ho and Mn) is angled at 60° with the z axis in $HoMn_6Ge_6$ [35]. In contrast, in RMn_6Sn_6 systems, the moments of R and Mn are aligned antiparallel to form a ferrimagnetic structure with an easy axis of magnetization angled with the z axis [23,29–31]. The angle between the z axis and the easy axis of magnetization strongly depends on the rare-earth element [23,29–31,35,36]. Further, as discussed in Ref. [35], the magnetic structure of these systems is very sensitive to the sample temperature. For instance, in the low-temperature region (<50 K), the Ho and Mn magnetic moments form a skew-spiral ($\widetilde{SS}$) structure coupled antiferromagnetically with a plane of moments making an angle θ_S with the z axis, producing finite net magnetization along both the in-plane and out-of-plane directions. However, as the temperature is increased, the skew-spiral structure gets distorted, and the other magnetic transitions emerge at 220 and 260 K. Beyond 260 K, the $\widetilde{SS}$ structure gets completely destroyed, and the system enters a cycloid state beyond 300 K [35].

In this work, high-quality single crystals of $HoMn_6Ge_6$ were grown using the Sn flux to study the magnetic and magnetotransport properties. Electrical resistivity demonstrates an overall metallic nature throughout the measured temperature range with a few magnetic transition-driven anomalies. A crossover from negative to positive magnetoresistance (MR) is observed at a critical temperature of 150 K. While the Dirac-like linear band dispersion mainly drives the linear nonsaturating positive MR in the low-temperature region, the negative MR observed in the higher-temperature region is due to the spin-flop-type magnetic transition. Most importantly, we identify a large anisotropy in the magnetoresistance due to

*setti@bose.res.in

the anisotropic Fermi surface present in this system. Further, we observe an anomalous Hall effect in addition to a switching of dominant charge carriers from electrons to holes at around 215 K, going from high to low temperatures. Also, we perform density functional theory calculations for $HoMn_6Ge_6$ by considering the experimentally obtained skew-spiral magnetic structure to understand our magnetotransport data better [35].

II. EXPERIMENTAL AND FIRST-PRINCIPLES CALCULATION DETAILS

Single crystals of $HoMn_6Ge_6$ were grown using Sn flux. First, Ho chunk (Alfa Aesar, 99.9%), Mn powder (Alfa Aesar, 99.95%), Ge powder (Alfa Aesar, 99.99%), and Sn shots (Alfa Aesar, 99.995%) were weighed in the ratio of 1:6:6:24. The mixture was kept in an alumina crucible, and we sealed the crucible together with the mixture inside an evacuated quartz ampoule. The mixture was heated up to 1000 °C at a rate of 50 °C/h and kept there for another 18 h, before the molten mixture was cooled down to 600 °C at a rate of 5 °C/h. Finally, the molten mixture was annealed for another 2 days at 600 °C. Then, the ampoule was quickly transferred to a centrifuge to separate the Sn flux from the samples. In this way, we obtained several hexagonal-shaped $HoMn_6Ge_6$ single crystals with a typical size of $(2 \times 2 \times 0.4\,\mathrm{mm}^3$, as shown in the inset of Fig. 1(a). X-ray diffraction (XRD) was done on flat-shaped single crystals and on the powders of crushed crystals using a Rigaku SmartLab with a 9 kW Cu $K\alpha$ x-ray source. The exact chemical composition of the as-grown single crystals was found using energy dispersive x-ray spectroscopy (EDXS). The electrical resistivity and magnetotransport measurements were performed using the four-probe and Hall-probe connections. Electrical, magnetic, and magnetotransport measurements were performed in a 9 T physical properties measurement system (DynaCool, Quantum Design) using the vibrating-sample magnetometer and Electrical transport option (ETO) options. To eliminate the longitudinal voltage contributions due to a possible misalignment of the Hall connections, the Hall resistivity was calculated using the relation $\frac{\rho_H(H)-\rho_H(-H)}{2}$.

To understand the magnetotransport properties, the electronic band structure of $HoMn_6Ge_6$ was calculated using the density-functional theory (DFT) within the Perdew-Burke-Ernzerhof-type generalized gradient approximation [37] as implemented in the QUANTUM ESPRESSO (QE) simulation package [38]. The electronic wave function is expanded using plane waves up to a cutoff energy of 100 Ry. Brillouin zone sampling is done over a $10 \times 10 \times 6$ Monkhorst-Pack k grid. The crystal structure was optimized through the variable-cell relaxation method as implemented in QE. Notably, the non-collinear skew-spiral magnetic structure was considered to determine the ground-state electronic properties. The band structure was produced with and without spin-orbit coupling (SOC).

III. RESULTS AND DISCUSSION

Figure 1(a) depicts the XRD pattern of the crushed $HoMn_6Ge_6$ single crystals overlapped by Rietveld refinement performed using the FULLPROF software. The Rietveld refinement confirms that $HoMn_6Ge_6$ crystallizes into the hexagonal kagome $HfFe_6Ge_6$-type crystal structure with a space group of $P6/mmm$ (No. 191). The refined lattice parameters $a = b = 5.2415(5)$ Å and $c = 8.1831(4)$ Å confirm that the studied sample of $HoMn_6Ge_6$ is almost equivalent to the reported ones within the error bars [33,35]. See Table I in the

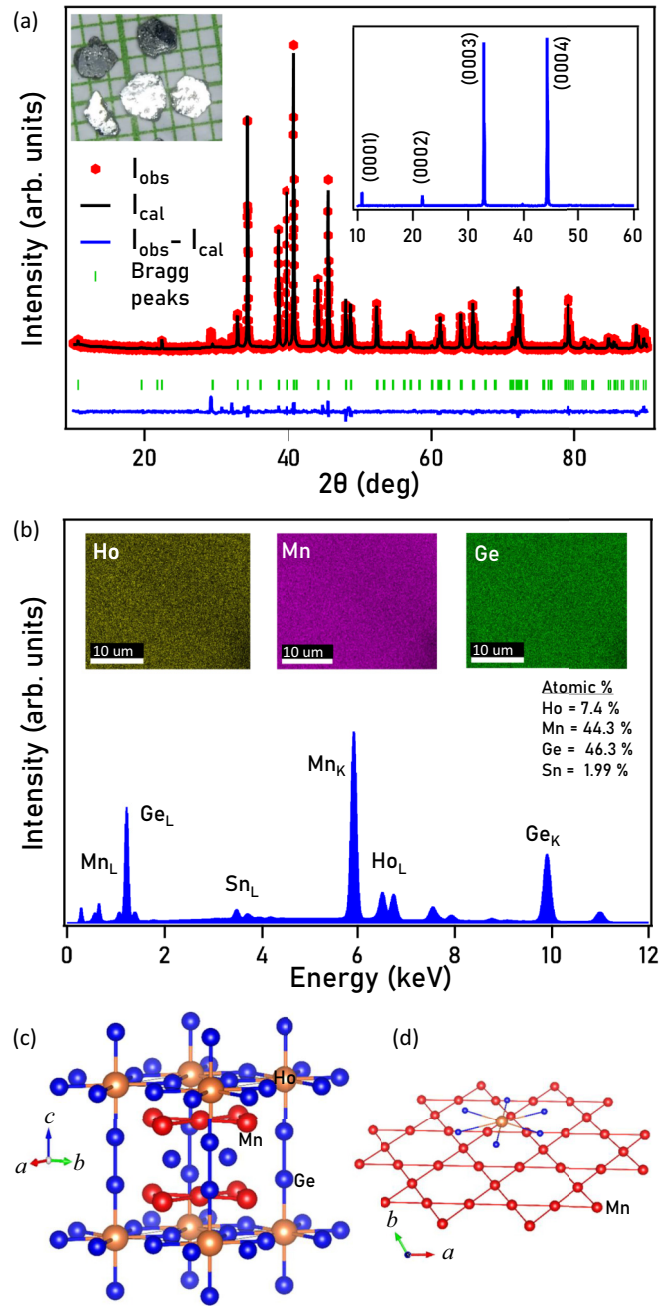

FIG. 1. (a) The powder XRD pattern of the crushed single crystals of $HoMn_6Ge_6$ overlapped by Rietveld refinement. The left inset in (a) shows an optical image of as-grown single crystals. The right inset in (a) represents the XRD pattern corresponding to the (000l) Bragg plane of the $HoMn_6Ge_6$ single crystal. (b) EDXS data for the $HoMn_6Ge_6$ single crystal. Insets in (b) show the elemental mapping of Ho, Mn, and Ge atoms. (c) Schematic representation of the primitive unit cell of $HoMn_6Ge_6$. (d) Kagome lattice plane formed by the Mn atoms when projected onto the ab plane.

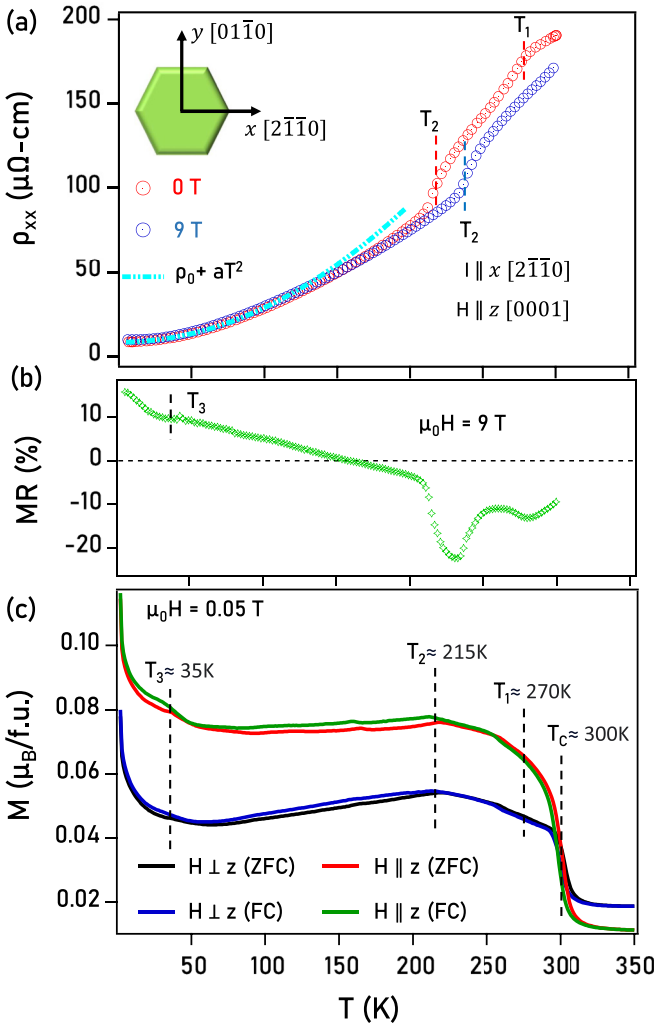

FIG. 2. (a) Longitudinal resistivity ρ_{xx} plotted as a function of temperature with current applied along the x [2$\bar{1}\bar{1}$0] axis for both 0 T (red curve) and 9 T (blue curve) fields applied along the z [0001] axis of the crystal. (b) Magnetoresistance MR(%) $= \frac{\rho_{xx}(9T)-\rho_{xx}(0T)}{\rho_{xx}(0T)} \times 100(\%)$ plotted as a function of temperature. (c) Magnetization plotted as a function of temperature [$M(T)$] for both the $H \parallel z$ and $H \perp z$ directions measured under field-cooled and zero-field-cooled modes with $\mu_0 H = 0.05$ T.

Supplemental Material [39] for a comparison of the structural parameters between our sample and similar compounds reported in Refs. [33,35]. The right inset in Fig. 1(a) shows the XRD pattern taken on the flat surface of the single crystal, confirming that the crystal growth plane is parallel to the (0001)-plane direction. Figure 1(b) depicts the EDXS data, confirming the exact chemical composition of the sample $Ho_{0.96}Mn_{5.74}Ge_6$. For convenience, hereafter, we represent it by the nominal composition of $HoMn_6Ge_6$. Since the crystals were grown using Sn flux, the crystals were found to have a maximum 2% Sn impurity. The elemental mappings done for Ho, Mn, and Ge, as shown in the top insets of Fig. 1(b), imply a good homogeneity of the studied single crystals.

Longitudinal electrical resistivity $\rho_{xx}(T)$ is plotted as a function of temperature, as shown in Fig. 2(a), measured without magnetic field (red data) and with magnetic field (blue data) applied parallel to the z axis [0001], with $\mu_0 H = 9$ T. The low-temperature resistivity (<100 K) can be reasonably fit with the quadratic equation for the Landau Fermi-liquid theory, $\rho_{xx}(T) = \rho_0 + \alpha T^2$. Here, $\rho_0 = 8.42$ μΩ cm is the residual resistivity due to impurity scattering, and $\alpha = 2 \times 10^{-9}$ μΩ cm/K^2 is the electron-electron scattering coefficient. Further, in the resistivity data ($\mu_0 H = 0$ T) we observe *kinks* at $T_1 \approx 270$ K and $T_2 \approx 215$ K. The transition temperatures T_1 and T_2 shift towards higher temperatures under the external magnetic fields. For instance, at a field of 9 T, the transition temperature T_2 shifted to 236 K, but we cannot identify T_1 under the 9 T field as the measurements were done only up to 300 K. This observation indicates the magnetic origin of the kinks. Further, the observation of the T_1 and T_2 transition temperatures under zero field is consistent with a previous report on $HoMn_6Ge_6$ in which the temperature range between T_1 and T_2 was referred to as a mixed magnetic state [$\widetilde{SS}$+antiferromagnetic (AFM)] [33]. Figure 2(b) depicts the magnetoresistance percentage (MR% $= [\rho_{xx}(T,H) - \rho_{xx}(T,0)]/\rho_{xx}(T,0)$] plotted as a function of temperature from which another transition is identified at $T_3 \approx 35$ K, although it is not clearly visible from the $\rho_{xx}(T)$ data [see Fig. 2(a)]. Overall, the longitudinal electrical resistivity shows the metallic nature throughout the measured temperature range with a residual resistivity ratio of $\rho_{xx}(300\text{ K})/\rho_{xx}(2\text{ K}) \approx 20$.

Figure 2(c) presents the magnetization plotted as a function of temperature $M(T)$ under magnetic field $\mu_0 H = 0.05$ T applied parallel ($H \parallel z$) and perpendicular ($H \perp z$) to the z axis, measured in both the field-cooled (FC) and zero-field-cooled (ZFC) modes. A clear overlap between the FC and ZFC data suggests that the magnetic moments are thermally reversible in the system throughout the measured temperature range of 2–350 K. On the other hand, a previous neutron diffraction study on a similar system revealed a complex magnetic structure with different magnetic states at different temperatures [35]. For instance, in the low-temperature region (<55 K), the Ho and Mn magnetic moments form a $\widetilde{SS}$ structure, coupled antiferromagnetically, with a plane of moments making an angle θ_S with the z axis [see Fig. 6(b) below], producing finite net magnetization along both the in-plane and out-of-plane directions. Between 55 and 220 K, both the wave vector q and phase angle ϕ_S increase monotonically with temperature. In the 220–260 K region, the $\widetilde{SS}$ structure gets distorted, accompanied by the Mn spin reorientation, thus eventually leading to a weak ferromagnetism at 300 K. Beyond 300 K the skew-spiral structure becomes a cycloid. In line with previous studies [33,35,40,41] we also observe magnetic transitions in the magnetization data at $T_1 \approx 270$ K, $T_2 \approx 215$ K, and $T_3 \approx 35$ K. Further, a weak ferromagneticlike magnetization jump is noticed at $T_C \approx 300$ K. As can be seen from Fig. 2(c), the out-of-plane magnetization ($H \parallel z$) is significantly higher than the in-plane magnetization ($H \perp z$) below 300 K, while the opposite is true above 300 K. This observation hints at the fluctuating magnetic moments across T_C. Also, note that a slight variation in the transition temperatures (T_1, T_2, and T_3) is noticed between our data and Refs. [33,35], possibly due to different sample preparation methods. Specifically, $M(T)$ of Ref. [33] shows a cusp at around 25 K and a rapid increase in $M(T)$ below 77 K, while no cusp is found but a rapid increase

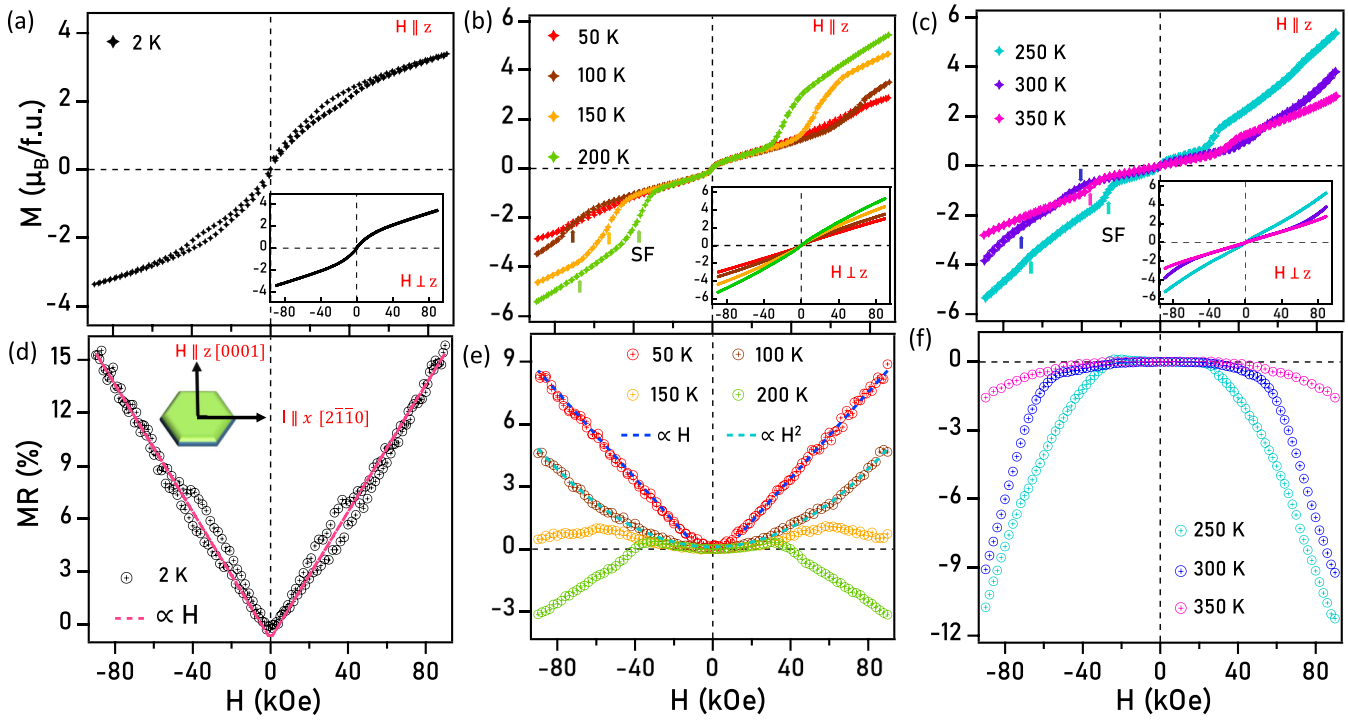

FIG. 3. (a)–(c) Isothermal magnetization $M(H)$ measured at different temperatures for the fields applied parallel to the z axis ($H \parallel z$). Insets in (a)–(c) show the same thing for $H \perp z$. (d)–(f) Field-dependent magnetoresistance [$\mathrm{MR}(\%) = \frac{\rho_{xx}(H)-\rho_{xx}(0)}{\rho_{xx}(0)} \times 100(\%)$] measured for different temperatures.

in $M(T)$ is found below 55 K in Ref. [35]. On the other hand, from our data we observe a cusp at 33 K and a rapid increase in $M(T)$ below 50 K [see Fig. 2(c)]. Similarly, the mixed magnetic state of AFM + $\widetilde{SS}$ is reported within the temperature range of 220–260 K in Ref. [35] and 215–245 K in Ref. [33], while in our data we find it in a broader temperature range of 215–270 K.

Next, Figs. 3(a)–3(c) depict magnetization isotherms $M(H)$ measured at different temperatures for $H \parallel z$ and $H \perp z$. We observe weak ferromagneticlike $M(H)$ data when they are measured at 2 K for both $H \parallel z$ and $H \perp z$ in lower-field regions without magnetization saturation. Further, field-induced hysteresis is visible for $H \parallel z$ between 2 and 4 T but not for $H \perp z$, possibly due to the out-of-plane spin canting within this field range. This type of metamagnetic state is not observed at higher temperatures. Instead, an out-of-plane spin-flop transition is found at a critical field H_{SF} that is temperature dependent, and as a result, a sudden increase in magnetization is noticed [see Figs. 3(b) and 3(c)]. However, the spin-flop transition is absent from the in-plane magnetization ($H \perp z$) at any measured temperature. A previous report also demonstrated similar spin-flop transitions in $HoMn_6Ge_6$ [33].

Isothermal MR at different sample temperatures and with the fields applied parallel to the z axis are shown in Figs. 3(d)–3(f). Figure 3(d) demonstrates the MR measured at 2 K, where the MR is linearly dependent (red dashed line) on the applied field in addition to the hysteresis between the 2 and 4 T fields that originate from the field-induced metamagnetic state [Fig. 3(a)]. From Fig. 3(e), we can see that the linear dependence of MR is intact up to 50 K. However, at 100 K, we observe a classical parabolic magnetoresistance. Although this parabolic nature is sustained at higher temperatures (150 and 200 K) as well, beyond the spin-flop (H_{SF}) transition, the MR starts to decrease with increasing field for a given temperature. Eventually, beyond H_{SF} the MR becomes negative above 150 K, consistent with the MR(T) data shown in Fig. 2(b), in which we can notice negative MR above 150 K when measured at 9 T. However, the MR becomes nearly field independent as the temperature reaches 350 K.

Overall, $HoMn_6Ge_6$ shows a complex temperature-dependent MR. Importantly, up to 50 K it shows a positive nonsaturating MR that is linearly dependent on the applied field. Several mechanisms explaining the linear MR exist, such as (1) the presence of linear dispersive Dirac-like bands with very low effective mass near the Fermi level in the case of topological materials [42,43], (2) a quasirandom resistor network model in the case of metal-semiconductor composites [44,45], and (3) carrier density fluctuations due to irregular current paths from the inhomogeneous or grain boundaries in the case of disordered systems [46,47]. We can safely rule out mechanism 2 as our system is not a metal-semiconductor composite. Also, since our studied system is in the single-crystalline form with no significant grain boundaries and with good homogeneity, we can rule out mechanism 3 as the origin of linear MR. Previous reports on its sister compounds RMn_6Sn_6 suggested that the linear MR could originate from the Dirac-like linear bands [29]. In addition, previous band structure calculations for these systems showed several Dirac-like linear band dispersions crossing the Fermi level [36,48]. To confirm that the linear MR originates from the linear Dirac-like topological band structure, we performed DFT calculation, which will be discussed later explicitly.

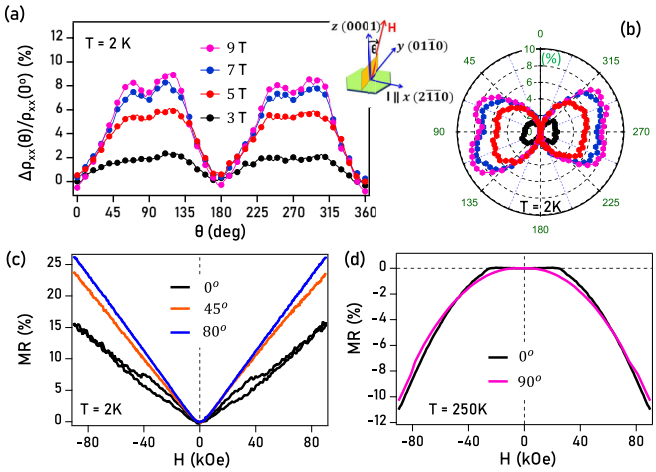

FIG. 4. (a) Angle-dependent magnetoresistance [ADMR(%) = $\frac{\rho_{xx}(\theta)-\rho_{xx}(0^\circ)}{\rho_{xx}(0^\circ)} \times 100(\%)$] measured for various applied fields at 2 K. The inset in (a) is a schematic showing the ADMR measuring geometry. Here θ is the angle between the z axis and the applied field direction. (b) is the same as (a), but plotted in polar coordinates for better visualization. In (b) the radius is the amplitude of ADMR(%). (c) Field-dependent MR measured at 2 K for different θ values. (d) is the same as (c), but measured at 250 K of the sample temperature.

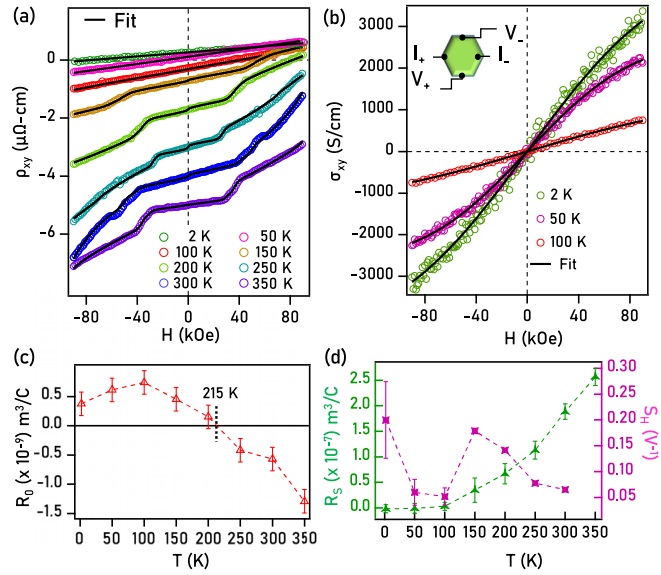

FIG. 5. (a) Field-dependent Hall resistivity ρ_{xy} measured for different sample temperatures overlapped by the fits (black curves). (b) Field-dependent Hall conductivity σ_{xy} plotted for 2, 50, and 100 K sample temperatures. The inset in (b) schematically shows the Hall effect measuring geometry. (c) Normal Hall coefficient R_0 plotted as a function of temperature. (d) Anomalous Hall coefficient R_S (left axis) and anomalous Hall scaling factor S_H (right axis) plotted as a function of temperature.

Further, we measured the angle-dependent magnetoresistance (ADMR) with the current and field directions always kept perpendicular to each other such that only the field direction changes with the crystal axes, as shown in the schematic in Fig. 4(a). The angle-dependent magnetoresistance is calculated as $\frac{\rho_{xx}(\theta)-\rho_{xx}(0^\circ)}{\rho_{xx}(0^\circ)}$ (%), while the applied magnetic field is kept constant. As seen from Fig. 4(a), at 2 K, the MR is positive for all the applied magnetic fields but very sensitive to the field angle, suggesting a strong anisotropic MR in this system. Specifically, MR is minimum at angles of 0°, 180°, and 360°, and it is maximum at angles of 60°, 120°, 240°, and 300°. Also, the saddle points in the ADMR are observed at 90° and 270° for all the applied fields. For a better visualization, we plot the ADMR in polar coordinates in Fig. 4(b), from which we can clearly observe a butterfly pattern for the out-of-plane MR at 2 K. It is worth mentioning here that the ADMR measured at 250 K is negligibly small (not shown) compared to the ADMR taken at 2 K. Next, Fig. 4(c) depicts the field-dependent MR plotted for different field angles (0°, 45°, and 80°) measured at 2 K, from which we observe linear MR at all field angles. Moreover, we see that the MR reaches almost 25% for $\theta = 80^\circ$, and the hysteresis, which was present for $\theta = 0^\circ$, has vanished at the other two angles. Figure 4(d) depicts field-dependent MR taken at 0° and 90° field angles, from which we observe the absence of a spin-flop transition effect on the MR when measured at 90°, consistent with $M(H)$ for $H \perp z$.

Next, Fig. 5(a) demonstrates field-dependent Hall resistivity [$\rho_{xy}(H)$] measured at different sample temperatures. We see a deviation in the Hall resistivity, leading to an anomalous Hall effect, at the spin-flop transition temperature. Usually, in ferromagnets, the Hall resistivity can be expressed as $\rho_H = R_0\mu_0 H + R_S\mu_0 M$ [49], where R_0 is the ordinary Hall coefficient and R_S is the anomalous Hall coefficient. Although the anomalous Hall effect (AHE) mainly appears in ferromagnets, recently, it was widely observed in noncollinear antiferromagnets as well [17,50–52]. From our Hall resistivity data, we can see that the anomalous Hall effect is induced by a spin-flop transition that resembles the $M(H)$ data shown in Figs. 3(a)–3(c). Moreover, the above formula can be rewritten as $\frac{\rho_H}{\mu_0 H} = R_0 + R_S\frac{M}{H}$, which imitates a linear equation, and the intercept on the y axis gives R_0, and slope gives the anomalous Hall coefficient R_S. Using this formalism, we reasonably fit the Hall resistivity as depicted in Fig. 5(a). The anomalous scaling factor S_H is calculated using the formula $S_H = \mu_0 R_S/\rho_{xx}^2$, where ρ_{xx} is the longitudinal resistivity. Figure 5(c) depicts the normal Hall coefficient R_0 plotted as a function of temperature. From Fig. 5(c), we further notice R_0 changing from positive to negative at around 215 K, which indicates hole-type (electron-type) carrier dominance below (above) 215 K.

As discussed above, a magnetic transition exists at around 215 K (T_2). It is possible that the change in magnetic structure influences the electronic structure near the Fermi level and thus the switching of charge carrier type at 215 K. This observation suggests a strong correlation between the magnetic and electronic structures in these systems. Moreover, the value of R_S decreases rapidly with decreasing temperature and becomes negligibly small below 100 K. However, S_H varies between 0.05 and 0.2 like in a typical ferromagnetic metal [49,53]. Further, from the relation $\mu_0 R_S = S_H\rho_{xx}^2$, it is clear that for very low resistivity ρ_{xx} values the contribution from AHE (R_S) is negligible, so only the ordinary Hall effect dominates at low temperatures. In Fig. 5(b), we plot the Hall conductivity as a function of temperature calculated using the

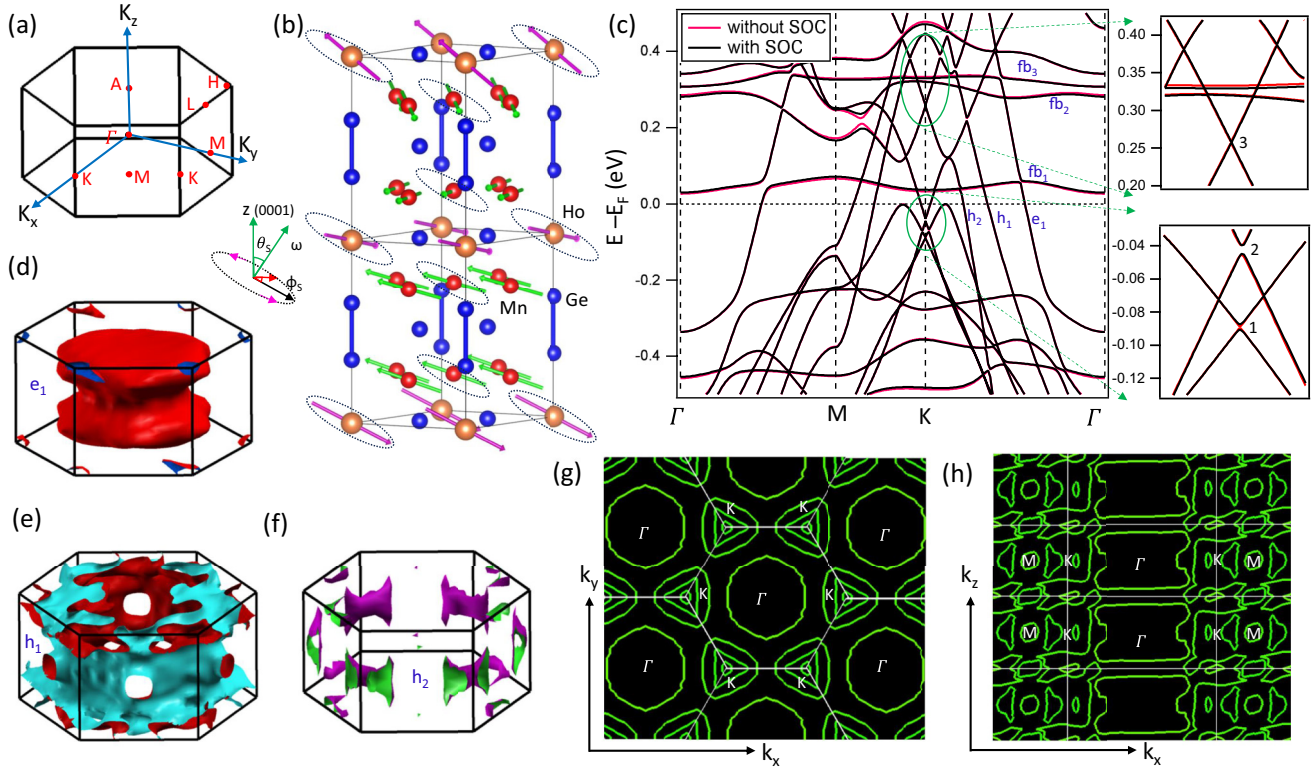

FIG. 6. (a) Hexagonal Brillouin zone showing the positions of various high-symmetry points. (b) Low-temperature skew-spiral ($\widetilde{SS}$) magnetic structure of $HoMn_6Ge_6$ [35]. Here, $\theta_s = 60^\circ$, and $\phi_s = 71.2^\circ$. (c) Electronic band structure of $HoMn_6Ge_6$ calculated for the magnetic configuration shown in (b) with (black) and without (red) the spin-orbit coupling (SOC). The right panels in (c) show the zoomed-in band structure to clearly display various Dirac points. (d)–(f) The calculated Fermi surface maps in three dimensions. (g) and (h) The constant-energy contours taken at the Fermi level in the $k_x - k_y$ and $k_x - k_z$ momentum planes, respectively.

formula $\sigma_{xy} = -\frac{\rho_{xy}}{\rho_{xy}^2+\rho_{xx}^2}$. In Fig. 5(b), we fit the Hall conductivity curves using the single-band model, $\sigma_{xy} = [\frac{n_h\mu_h{}^2}{1+(\mu_h B)^2}]eB$, because at low temperatures the hole carriers dominate the total Hall transport. Here, n_h is hole carrier density, and μ_h is hole mobility. From the fits, we derive that the hole carrier concentration of n_h is 1.06×10^{20} cm^{-3} and hole mobility is $\mu = 0.049$ m^2/Vs at 2 K. These values are consistent with a previous report on these types of systems [29].

To uncover the mechanism of unsaturated linear MR, we perform density functional theory calculations, as illustrated in Fig. 6. For the DFT calculations, we consider the magnetic structure shown in Fig. 6(b), depicted by the neutron diffraction study on this system [35]. Figure 6(c) displays the electronic band dispersion along the high-symmetry k path of Γ-M-K-Γ calculated without and with SOC. We notice several linear band crossings (Dirac-like) from the electronic band structure at the K point near the Fermi level. One Dirac point (DP1) is observed at a binding energy of 90 meV below the Fermi level E_F and is gapless without SOC, but under SOC, the Dirac point is gapped by lifting the degeneracy. DP2 is found at a binding energy of 40 meV below E_F and is always gaped. DP3 is found at a binding energy of 250 meV above E_F and is gapless both with SOC and without SOC. Our calculations for $HoMn_6Ge_6$ align with previous calculations performed for $HoMn_6Sn_6$ [31,36]. Particularly, the calculations for $HoMn_6Sn_6$ demonstrated that gap size at the Dirac points depends explicitly on the magnetic spin orientation with respect to the crystal axis [31,36]. This means larger (smaller) gaps were predicted for the fields applied along the out-of-plane (in-plane) direction. Since our calculations were performed with an angle of $\theta_S = 60^\circ$ between the z axis and plane of magnetic moments, which is neither out of plane nor in plane, we observe both gapped and gapless Dirac points. This observation hints at the possibility of a critical angle of magnetic moments at which the Dirac states are gapless and robust under SOC.

Apart from the linear band dispersions at the K point, we also observe two holelike band dispersions (h_1 and h_2) crossing the Fermi level around the K point and an electronlike (e_1) band dispersion crossing the Fermi level around the Γ point. No bands are found at the M point crossing the Fermi level. In addition, we find several flat bands (fb_1, fb_2, and fb_3) that are dispersionless throughout the Brillouin zone. Figures 6(d)–6(f) show a three-dimensional view of the Fermi surface maps, which are mainly contributed by three types of Fermi pockets: one of them is the electronlike (e_1) pocket with an almost cylindrical shape, as shown in Fig. 6(d); the second one is the holelike (h_1) pocket, which is close to one third of a cylinder shared by each corner of the hexagon, as shown in Fig. 6(e); and the last one is the hip-roof-shaped holelike (h_2) pocket at the K point. With the help of these three types of Fermi pockets, we estimate the hole carrier density $n_h = 5.3 \times 10^{20}$/cm^3 and electron carrier density $n_e = 3.6 \times 10^{20}$/cm^3 to find a net hole carrier density of 1.7×10^{20}/cm^3 using Luttinger's theorem [54] (see the Supplemental Material

[39]). Interestingly, this value is close to the experimentally calculated net carrier density (1.06×10^{20} cm^{-3}) from the Hall data at 2 K. The estimated hole and electron carrier densities are nearly equal, suggesting a possible charge compensation in this system [55,56]. Further, the estimated net carrier density of 1.06×10^{20} cm^{-3} suggests $HoMn_6Ge_6$ is a semimetal [57,58]. Figures 6(g) and 6(h) illustrate the Fermi surfaces projected onto the k_x-k_y and k_x-k_z planes, clearly showing the electronlike Fermi pocket at Γ and holelike Fermi pockets at the K point.

As for the ADMR measurements, the magnetic field is always perpendicular to the current direction, which does not change the Lorentz force acting on the charge carriers. The spin-charge scattering can be neglected at low temperatures as the mean free path of the charge carriers is much higher in this system at 2 K (≈0.67 μm) compared to the distance of Mn-Mn (2.62 Å) or Ho-Ho (5.24 Å) magnetic moments. This leads us to conclude that the anisotropic ADMR has an electronic band structure origin rather than a magnetism origin. The Fermi velocity can be calculated as $v_k = \frac{1}{\hbar}\nabla_k \epsilon_k$, which depends on the local curvature of the Fermi surface cross section. The smaller the orbit of the Fermi surface cross section is, the greater the local curvature is, leading to a higher Fermi velocity. Hence, a high microscopic Lorentz force would act on the charge carriers [59–61]. Our calculations indicate that the electron pocket e_1 and hole pocket h_1 exhibit nearly cylindrical shapes, with their diameters and heights being quite similar in value, making them nearly isotropic. Only the h_2 hole pocket has an anisotropic shape (hip roof shaped), which could be the possible origin of this high anisotropic ADMR when the field is applied along the z axis, the charge carriers are subjected to an orbit on the k_x-k_y plane. Similarly, for fields applied along the y axis the carriers would orbit on the k_x-k_z plane. As observed in Fig. 6(g), the Fermi sheets at the K point are nearly circular for $H \parallel z$ [see Fig. 4(a) for $\theta = 0°$]. Only the out-of-plane Fermi sheets (k_x-k_z) have substantial curvature [see Fig. 6(h)], which is detected experimentally for $H \parallel y$ [see Fig. 4(a) for $\theta = 90°$]. Therefore, we think the asymmetric MR originates from the asymmetric out-of-plane Fermi pockets. Further, as evidenced by our DFT band structure calculations, the linear nonsaturating MR is mainly contributed by the linear Dirac-like bands near the Fermi level.

IV. SUMMARY

In summary, using Sn flux, we grew high-quality single crystals of $HoMn_6Ge_6$. Electrical resistivity, with a few magnetic transition-driven anomalies, demonstrated an overall metallic nature throughout the measured temperature range. A crossover from negative to positive MR was observed at a critical temperature of 150 K. While the Dirac-like linear band dispersions mainly drive the linear nonsaturating positive MR exists in the low-temperature region, the negative MR observed in the higher-temperature region is due to the spin-flop-type magnetic transition. We found an anomalous Hall effect in addition to a dominant charge carrier switching across 215 K. We performed electronic band structure calculations on $HoMn_6Ge_6$ by considering the skew-spiral magnetic structure of the system to realize large anisotropy in the out-of-plane Fermi sheets. We suggest that the large anisotropic out-of-plane magnetoresistance observed in $HoMn_6Ge_6$ originates from the anisotropic out-of-plane Fermi surfaces. The band structure calculations predict several Dirac-type band crossings at the K point near the Fermi level.

ACKNOWLEDGMENTS

This research used the Technical Research Centre (TRC) Instrument Facilities of S. N. Bose National Centre for Basic Sciences, established under the TRC project of the Department of Science and Technology, Government of India .

[1] M. S. S. Brooks, L. Nordström, and B. Johansson, Rare-earth transition-metal intermetallics, Phys. B (Amsterdam, Neth.) **172**, 95 (1991).

[2] F. D. M. Haldane, Model for a quantum Hall effect without Landau levels: Condensed-matter realization of the "parity anomaly," Phys. Rev. Lett. **61**, 2015 (1988).

[3] C. Z. Chang *et al.*, Experimental observation of the quantum anomalous Hall effect in a magnetic topological insulator, Science **340**, 167 (2013).

[4] B. Keimer and J. E. Moore, The physics of quantum materials, Nat. Phys. **13**, 1045 (2017).

[5] S. Sachdev, Topological order, emergent gauge fields, and Fermi surface reconstruction, Rep. Prog. Phys. **82**, 014001 (2019).

[6] Y. Tokura, K. Yasuda, and A. Tsukazaki, Magnetic topological insulators, Nat. Rev. Phys. **1**, 126 (2019).

[7] P. C. Canfield, New materials physics, Rep. Prog. Phys. **83**, 016501 (2020).

[8] A. Hirohata, K. Yamada, Y. Nakatani, I. L. Prejbeanu, B. Dieny, P. Pirro, and B. Hillebrands, Review on spintronics: Principles and device applications, J. Magn. Magn. Mater. **509**, 166711 (2020).

[9] A. Kitaev, Anyons in an exactly solved model and beyond, Ann. Phys. (NY) **321**, 2 (2006).

[10] J. S. Helton, K. Matan, M. P. Shores, E. A. Nytko, B. M. Bartlett, Y. Yoshida, Y. Takano, A. Suslov, Y. Qiu, J.-H. Chung, D. G. Nocera, and Y. S. Lee, Spin dynamics of the spin-1/2 kagome lattice antiferromagnet $ZnCu_3(OH)_6Cl_2$, Phys. Rev. Lett. **98**, 107204 (2007).

[11] T. Han, J. S. Helton, S. Chu, D. G. Nocera, J. A. Rodriguez-Rivera, C. Broholm, and Y. S. Lee, Fractionalized excitations in the spin-liquid state of a kagome-lattice antiferromagnet, Nature (London) **492**, 406 (2012).

[12] Y. Kasahara, T. Ohnishi, Y. Mizukami, O. Tanaka, S. Ma, K. Sugii, N. Kurita, H. Tanaka, J. Nasu, Y. Motome, T. Shibauchi, and Y. Matsuda, Majorana quantization and half-integer thermal quantum Hall effect in a Kitaev spin liquid, Nature (London) **559**, 227 (2018).

[13] B. Sutherland, Localization of electronic wave functions due to local topology, Phys. Rev. B **34**, 5208 (1986).

[14] D. Leykam, A. Andreanov, and S. Flach, Artificial flat band systems: From lattice models to experiments, Adv. Phys.: X **3**, 1473052 (2018).

[15] M. Kang *et al.*, Dirac fermions and flat bands in the ideal kagome metal FeSn, Nat. Mater. **19**, 163 (2020).

[16] M. Kang, S. Fang, L. Ye, H. C. Po, J. D. Denlinger, C. Jozwiak, A. Bostwick, E. Rotenberg, E. Kaxiras, J. Checkelsky, and R. Comin, Topological flat bands in frustrated kagome lattice CoSn, Nat. Commun. **11**, 4004 (2020).

[17] S. Nakatsuji, N. Kiyohara, and T. Higo, Large anomalous Hall effect in a non-collinear antiferromagnet at room temperature, Nature (London) **527**, 212 (2015).

[18] K. Kuroda *et al.*, Evidence for magnetic Weyl fermions in a correlated metal, Nat. Mater. **16**, 1090 (2017).

[19] E. Liu, Y. Sun, N. Kumar, L. Muechler, A. Sun, L. Jiao, S. Yang, D. Liu, A. Liang, Q. Xu, J. Kroder, V. Süß, H. Borrmann, C. Shekhar, Z. Wang, C. Xi, W. Wang, W. Schnelle, S. Wirth, Y. Chen, S. T. B. Goennenwein, and C. Felser, Giant anomalous Hall effect in a ferromagnetic kagome-lattice semimetal, Nat. Phys. **14**, 1125 (2018).

[20] L. Ye, M. Kang, J. Liu, F. Von Cube, C. Wicker, T. Suzuki, C. Jozwiak, A. Bostwick, E. Rotenberg, D. C. Bell, L. Fu, R. Comin, and J. Checkelsky, Massive Dirac fermions in a ferromagnetic kagome metal, Nature (London) **555**, 638 (2018).

[21] D. F. Liu, A. Liang, E. K. Liu, Q. Xu, Y. W. Li, C. Chen, D. Pei, W. Shi, S.-K. Mo, P. Dudin, T. K. Kim, C. Cacho, G. Li, Y. Sun, L. Yang, Z. K. Liu, S. S. P. Parkin, C. Felser, and Y. L. Chen, Magnetic Weyl semimetal phase in a kagomé crystal, Science **365**, 1282 (2019).

[22] G. Xu, B. Lian, and S.-C. Zhang, Intrinsic quantum anomalous Hall effect in the kagome lattice $Cs_2LiMn_3F_{12}$, Phys. Rev. Lett. **115**, 186802 (2015).

[23] J.-X. Yin *et al.*, Quantum-limit Chern topological magnetism in $TbMn_6Sn_6$, Nature (London) **583**, 533 (2020).

[24] M. Hirschberger, T. Nakajima, S. Gao, L. Peng, A. Kikkawa, T. Kurumaji, M. Kriener, Y. Yamasaki, H. Sagayama, H. Nakao, K. Ohishi, K. Kakurai, Y. Taguchi, X. Yu, T.-H. Arima, and Y. Tokura, Skyrmion phase and competing magnetic orders on a breathing kagomé lattice, Nat. Commun. **10**, 5831 (2019).

[25] D. Chakrabartty, S. Jamaluddin, S. K. Manna, and A. K. Nayak, Tunable room temperature magnetic skyrmions in centrosymmetric kagome magnet Mn_4Ga_2Sn, Commun. Phys. **5**, 189 (2022).

[26] T. Chen, T. Tomita, S. Minami, M. Fu, T. Koretsune, M. Kitatani, M. Ikhlas, D. Nishio-Hamane, R. Ishii, F. Ishii, R. Arita, and S. Nakatsuji, Anomalous transport due to Weyl fermions in the chiral antiferromagnets Mn_3X, $X =$ Sn, Ge, Nat. Commun. **12**, 572 (2021).

[27] T. Chen, S. Minami, A. Sakai, Y. Wang, Z. Feng, T. Nomoto, M. Hirayama, R. Ishii, T. Koretsune, R. Arita, and S. Nakatsuji, Large anomalous Nernst effect and nodal plane in an iron-based kagome ferromagnet, Sci. Adv. **8**, eabk1480 (2022).

[28] Z. Hou, W. Ren, B. Ding, G. Xu, Y. Wang, B. Yang, Q. Zhang, Y. Zhang, E. Liu, F. Xu, W. Wang, G. Wu, X. Zhang, B.-G. Shen, and Z. Zhang, Observation of various and spontaneous magnetic skyrmionic bubbles at room temperature in a frustrated kagome magnet with uniaxial magnetic anisotropy, Adv. Mater. **29**, 1701144 (2017).

[29] W. Ma, X. Xu, J.-X. Yin, H. Yang, H. Zhou, Z.-J. Cheng, Y. Huang, Z. Qu, F. Wang, M. Z. Hasan, and S. Jia, Rare earth engineering in RMn_6Sn_6 ($R =$ Gd–Tm, Lu) topological kagome magnets, Phys. Rev. Lett. **126**, 246602 (2021).

[30] L. Gao, S. Shen, Q. Wang, W. Shi, Y. Zhao, C. Li, W. Cao, C. Pei, J.-Y. Ge, G. Li, J. Li, Y. Chen, S. Yan, and Y. Qi, Anomalous Hall effect in ferrimagnetic metal RMn_6Sn_6 ($R =$ Tb, Dy, Ho) with clean Mn kagome lattice, Appl. Phys. Lett. **119**, 092405 (2021).

[31] F. Kabir, R. Filippone, G. Dhakal, Y. Lee, N. Poudel, J. Casey, A. P. Sakhya, S. Regmi, R. Smith, P. Manfrinetti, L. Ke, K. Gofryk, M. Neupane, and A. K. Pathak, Unusual magnetic and transport properties in $HoMn_6Sn_6$ kagome magnet, Phys. Rev. Mater. **6**, 064404 (2022).

[32] D. Campbell, J. Collini, J. Sławińska, C. Autieri, L. Wang, K. Wang, B. Wilfong, Y. S. Eo, P. M. Neves, D. Graf, E. E. Rodriguez, N. P. Butch, M. B. Nardelli, and J. Paglione, Topologically driven linear magnetoresistance in helimagnetic FeP, npj Quantum Mater. **6**, 38 (2021).

[33] H. Zhou, M. Shi, Y. Huang, W. Ma, X. Xu, J. Wang, and S. Jia, Metamagnetic transition and anomalous Hall effect in Mn-based kagomé magnets RMn_6Ge_6($R =$ Tb-Lu), Phys. Rev. Mater. **7**, 024404 (2023).

[34] G. Venturini, R. Welter, and B. Malaman, Crystallographic data and magnetic properties of RT_6Ge_6 compounds (R Sc, Y, Nd, Sm, Gd Lu; T Mn, Fe), J. Alloys Compd. **185**, 99 (1992).

[35] P. Schobinger-Papamanteilos, A neutron diffraction study of the magnetic ordering of $HoMn_6Ge_6$, J. Magn. Magn. Mater. **139**, 119 (1995).

[36] Y. Lee, R. Skomski, X. Wang, P. P. Orth, Y. Ren, B. Kang, A. K. Pathak, A. Kutepov, B. N. Harmon, R. J. McQueeney, I. I. Mazin, and L. Ke, Interplay between magnetism and band topology in the kagome magnets RMn_6Sn_6, Phys. Rev. B **108**, 045132 (2023).

[37] J. P. Perdew, K. Burke, and M. Ernzerhof, Generalized gradient approximation made simple, Phys. Rev. Lett. **77**, 3865 (1996).

[38] P. Giannozzi *et al.*, QUANTUM ESPRESSO: A modular and open-source software project for quantum simulations of materials, J. Phys.: Condens. Matter **21**, 395502 (2009).

[39] See Supplemental Material at http://link.aps.org/supplemental/10.1103/PhysRevB.109.195104 for additional structural information.

[40] G. Venturini, A. Vernière, and B. Malaman, Multi spin-reorientation process in $HfFe_6Ge_6$-type $HoMn_6Ge_{6-x}Ga_x$ compounds (x = 0.2, 0.4, 1.0), J. Alloys Compd. **320**, 46 (2001).

[41] A. Mar, C. Lefèvre, and G. Venturini, Anisotropic transport properties measured in $HoMn_6Ge_6$ single crystals, J. Magn. Magn. Mater. **269**, 380 (2004).

[42] A. A. Abrikosov, Quantum magnetoresistance, Phys. Rev. B **58**, 2788 (1998).

[43] A. A. Abrikosov, Quantum linear magnetoresistance, Europhys. Lett. **49**, 789 (2000).

[44] J.-P. Xu, Z. Duan-Ming, Z. Deng, Y. Fu, Z. Li, and Y. Pan, Quasi-random resistor network model for linear magnetoresistance of metal–semiconductor composite, Chin. Phys. Lett. **25**, 4124 (2008).

[45] N. Ramakrishnan, Y. T. Lai, S. Lara, M. M. Parish, and S. Adam, Equivalence of effective medium and random resistor network models for disorder-induced unsaturating linear magnetoresistance, Phys. Rev. B **96**, 224203 (2017).

[46] R. Xu, A. Husmann, T. F. Rosenbaum, M.-L. Saboungi, J. E. Enderby, and P. B. Littlewood, Large magnetoresistance in non-magnetic silver chalcogenides, Nature (London) **390**, 57 (1997).

[47] M. M. Parish and P. B. Littlewood, Non-saturating magnetoresistance in heavily disordered semiconductors, Nature (London) **426**, 162 (2003).

[48] G. Dhakal, F. Cheenicode Kabeer, A. K. Pathak, F. Kabir, N. Poudel, R. Filippone, J. Casey, A. Pradhan Sakhya, S. Regmi, C. Sims, K. Dimitri, P. Manfrinetti, K. Gofryk, P. M. Oppeneer, and M. Neupane, Anisotropically large anomalous and topological Hall effect in a kagome magnet, Phys. Rev. B **104**, L161115 (2021).

[49] N. Nagaosa, J. Sinova, S. Onoda, A. H. MacDonald, and N. P. Ong, Anomalous Hall effect, Rev. Mod. Phys. **82**, 1539 (2010).

[50] Y. Luo, F. Ronning, N. Wakeham, X. Lu, T. Park, Z.-A. Xu, and J. D. Thompson, Pressure-tuned quantum criticality in the antiferromagnetic Kondo semimetal $CeNi_{2-\delta}As_2$, Proc. Natl. Acad. Sci. USA. **112**, 13520 (2015).

[51] T. Suzuki, R. Chisnell, A. Devarakonda, Y.-t. Liu, F. Wang, D. Xiao, J. W. Lynn, and J. Checkelsky, Large anomalous Hall effect in a half-Heusler antiferromagnet, Nat. Phys. **12**, 1119 (2016).

[52] J. Niu, B. Yan, Q. Ji, Z. Liu, M. Li, P. Gao, Y. Zhang, D. Yu, and X. Wu, Anomalous Hall effect and magnetic orderings in nanothick V_5S_8, Phys. Rev. B **96**, 075402 (2017).

[53] Q. Wang, S. Sun, X. Zhang, F. Pang, and H. Lei, Anomalous Hall effect in a ferromagnetic Fe_3Sn_2 single crystal with a geometrically frustrated Fe bilayer kagome lattice, Phys. Rev. B **94**, 075135 (2016).

[54] J. M. Luttinger, Fermi surface and some simple equilibrium properties of a system of interacting fermions, Phys. Rev. **119**, 1153 (1960).

[55] M. N. Ali, J. Xiong, S. Flynn, J. Tao, Q. Gibson, L. M. Schoop, T. Liang, N. Haldolaarachchige, M. Hirschberger, N. P. Ong, and R. J. Cava, Large, non-saturating magnetoresistance in WTe_2, Nature (London) **514**, 205 (2014).

[56] S. Thirupathaiah, R. Jha, B. Pal, J. S. Matias, P. K. Das, I. Vobornik, R. A. Ribeiro, and D. D. Sarma, Temperature-independent band structure of WTe_2 as observed from angle-resolved photoemission spectroscopy, Phys. Rev. B **96**, 165149 (2017).

[57] Y. Qi *et al.*, Superconductivity in Weyl semimetal candidate $MoTe_2$, Nat. Commun. **7**, 11038 (2016).

[58] S. Thirupathaiah, R. Jha, B. Pal, J. S. Matias, P. K. Das, P. K. Sivakumar, I. Vobornik, N. C. Plumb, M. Shi, R. A. Ribeiro, and D. D. Sarma, $MoTe_2$: An uncompensated semimetal with extremely large magnetoresistance, Phys. Rev. B **95**, 241105(R) (2017).

[59] A. Collaudin, B. Fauqué, Y. Fuseya, W. Kang, and K. Behnia, Angle dependence of the orbital magnetoresistance in bismuth, Phys. Rev. X **5**, 021022 (2015).

[60] J. Wang, H. Yang, L. Ding, W. You, C. Xi, J. Cheng, Z. Shi, C. Cao, Y. Luo, Z. Zhu, J. Dai, M. Tian, and Y. Li, Angle-dependent magnetoresistance and its implications for Lifshitz transition in W_2As_3, npj Quantum Mater. **4**, 58 (2019).

[61] S. N. Zhang, Q. S. Wu, Y. Liu, and O. V. Yazyev, Magnetoresistance from Fermi surface topology, Phys. Rev. B **99**, 035142 (2019).